2 (2026) 100017

Contents lists available at ScienceDirect

EANM Innovation

journal homepage: www.elsevier.com/locate/eanmi

In vivo voxel-wise positronium lifetime imaging of thyroid cancer using clinically routine I-124 PET/CT

Lorenzo Mercolli [a,b,c,*], William M. Steinberger [d], Tilman Läppchen [a], Michelle Amon [a], Carola Bregenzer [a], Maurizio Conti [d], Ângelo R. Felgosa Cardoso [a], Clemens Mingels [a], Paweł Moskal [e,f], Narendra Rathod [a,b], Hasan Sari [a,b,g], Ewa Ł. Stępień [e,f], Sabine Weidner [a], Axel Rominger [a], Kuangyu Shi [a,b,h], Robert Seifert [a,h]

[a] Department of Nuclear Medicine, Inselspital, Bern University Hostpital, University of Bern, Bern, Switzerland
[b] ARTORG Center for Biomedical Engineering Research, University of Bern, Bern, Switzerland
[c] Albert Einstein Center for Fundamental Physics (AEC), Laboratory for High Energy Physics (LHEP), University of Bern, Bern, Switzerland
[d] Siemens Medical Solutions USA, Inc., 810 Innovation Drive, Knoxville TN, USA
[e] Faculty of Physics, Astronomy and Applied Computer Scienc, Jagiellonian University, Krakow, Poland
[f] Centre for Theranostics, Jagiellonian University, Krakow, Poland
[g] Siemens Healthineers International AG, Zürich, Switzerland
[h] shared contribution,

ARTICLE INFO

Keywords:
Positronium
Long axial field-of-view PET/CT
[^{124}I]NaI
Thyroid cancer

ABSTRACT

Purpose: Measuring the lifetime of orthopositronium (oPs) has emerged as a promising approach for assessing tumor microenvironment characteristics, leveraging the susceptibility of oPs lifetime to local molecular factors. This study investigates the feasibility of voxel-wise oPs lifetime measurements in patients with thyroid cancer using a commercial long axial field-of-view (LAFOV) PET/CT scanner.

Methods: Three patients with thyroid cancer underwent two PET/CT scans at 2 and 26 h post-administration [^{124}I]NaI, which included a 30 min scan in singles mode that allows to identify three-photon events. For regions with high ^{124}I uptake, we determined the lifetime of oPs through a Bayesian fit for a voxel-based (with a voxel size of $7 \times 7 \times 7$ mm^3), lesion-based and organ-based analysis.

Results: The oPs lifetime of the voxel with the highest count statistics and activity concentration of 108.1 kBq mL^{-1} is 1.77 ± 0.26 ns. The visualization of the oPs lifetimes inside a lesion was feasible, though it remains affected by statistical uncertainty. On a per-lesion basis, the lifetime could be measured (exemplary lesion:1.90 ± 0.17 ns) with mean activity concentrations ranging from 9.5 to 34.1 kBq mL^{-1} and volumes of 1.31 to 6.27 mL. The positronium lifetime measurement error shows a slight correlation (r=0.48 with BF_{10}=7.88) with activity concentration of the regarded region. Besides lesions, the positronium lifetime could also be determined in several organs.

Conclusion: This is the first report of human in-vivo measurement of oPs lifetime with [^{124}I]NaI using a commercial LAFOV PET/CT scanner. The voxel-wise oPs lifetime imaging is feasible, though with a high statistical uncertainty. Lesion-based measurements can yield satisfactory statistical precision even for small volumes.

Introduction

Conventional positron emission tomography (PET) traditionally relies on the detection of two 511 keV annihilation photons to map the spatial distribution of radiotracers in the human body. Recently, after invention of positronium imaging [1,2], there has been significant interest to go beyond standard coincidence PET imaging by measuring the lifetime of orthopositronium (oPs) - a bound state of an electron and a positron with spin 1 - in human tissue [1,3–19]. The lifetime of oPs varies due to interaction with surrounding tissue. This dependence on the local molecular environment makes oPs lifetime measurements a tool for assessing microenvironmental features and potentially provide an additional diagnostic information. On the other hand, parapositronium (pPs) is short lived (about 0.124 ns lifetime) and does not interact significantly with its environment.

Last year, Ref. [20] presented the first patient study using the prototype scanner J-PET. Refs. [21–24] showed that in vivo oPs lifetime

* Corresponding author at: Department of Nuclear Medicine, Inselspital, Bern University Hostpital, University of Bern, Bern, Switzerland.
E-mail address: lorenzo.mercolli@insel.ch (L. Mercolli).

https://doi.org/10.1016/j.eanmi.2025.100017
Received 22 August 2025; Received in revised form 27 October 2025; Accepted 30 October 2025
Available online 10 December 2025

List of abbreviations

3γE	Three-photon events
BR	Branching ratio
CT	Computed tomography
HDI	Highest-density-interval
LAFOV	Long axial field-of-view
oPs	Orthopositronium
oPsLI	Orthopositronium lifetime imaging
PAL	Positron annihilation lifetime
PALS	Positron annihilation lifetime spectroscopy
PET	Positron emission tomography
pPs	Parapositronium
SUV	Standardized uptake value
TOF	Time-of-flight
VOI	volume-of-interest

measurements are possible on a commercial long axial field-of-view (LAFOV) PET/CT. However, measuring oPs lifetimes in a clinical setting has proven challenging. Measuring the oPs lifetime through positron annihilation lifetime spectroscopy (PALS) (see e.g. [11,12,25]) requires the detection of two annihilation photons and a prompt photon from the same nuclear decay/deexcitation, i.e. three-photon events (3γE). The measured time differences between the prompt photon and the two annihilation photons in each 3γE contain the oPs lifetime. Fitting a model to the histogram of these time differences allows to disentangle the oPs lifetime from other annihilation pathways. Non-pure positron emitting radionuclides that are used in clinical routine have rather small prompt-photon branching ratios (BR) since in standard PET imaging, the prompt photons are considered nuisance that needs to be corrected [26]. Despite the increased sensitivity that long axial field-of-view PET/CT scanners provide [27–29], the methodology of Ref. [21] for selecting 3γE in conjunction with the restricted energy range of the scanner available to Refs. [22–24] is limited by count statistics. From these studies, ^{124}I has crystallized as the most promising candidate for PALS measurements with a commercial PET/CT due to its prompt photon energy of 602.73 ± 0.08 keV with a reasonably high BR of 62.9 ± 0.7 % (which reduces to 12.0 ± 1.1 % when electron capture decays are removed).

Refs. [1,4] proposed positronium lifetime imaging (oPsLI), i.e. spatially binning 3γE and determining the oPs lifetime through PALS in individual voxels. The voxel values of the resulting image is the oPs lifetime. oPsLI therefore allows to visualize the spatial variation of the oPs lifetime. The image reconstruction process for oPsLI has triggered substantial research and alternative event selection and more refined image reconstruction techniques [10,16–19,30–32] may in the future alleviate the limitation of the current methodology of Ref. [21].

In a phantom study Ref. [23] showed that oPsLI is feasible with ^{124}I on a commercial PET/CT scanner using the methodology of Ref. [21]. As shown in Refs. [21–24], the Biograph Vision Quadra (Siemens Healthineers, Knoxville TN, USA) can optimally exploit ^{124}I's physical properties, which is not the case for high-energy prompt photon emitting radionuclides like ^{68}Ga, ^{82}Rb or ^{44}Sc. Apart from the technical capabilities of Quadra, the differentiation of thyroid cancer may be associated with tumor hypoxia [33,34] and therefore has the potential to provide an excellent clinical application for oPsLI using ^{124}I. Through an early and a late scan of three patients, we investigate the oPs lifetime in organs and tumor lesions. Despite low statistical precision, we construct oPsLI for the most emblematic cases.

Materials and methods

This study included three patients with thyroid carcinoma who have been referred to ^{131}I-therapy for initial ablation after thyroidectomy (S1) or because of recurrent thyroid cancer (S2 and S3) with rising thyreoglobulin levels. The ^{124}I PETs were performed as part of routine clinical practice for staging and to assess the extent of postsurgical remnant tissue (S1) and/or to plan the ^{131}I therapy dose (S2, S3). Patients presented with follicular thyroid cancer and cervical lymph node metastases (S1), poorly differentiated thyroid cancer with a bone metastasis that showed intense uptake on [^{18}F]FDG (S2), and papillary thyroid cancer with a recently resected lung metastasis (S3). Data analysis was done retrospectively.

The three patients received an oral capsule of ^{124}I sodium iodide (3D Imaging LLC, Little Rock, AR, USA). The administered activity was 41.02 MBq, 40.11 MBq and 39.44 MBq, respectively, and the patients were scanned at 2 h and at 26 h post application on a LAFOV PET/CT. The early and late scan followed the same protocol, i.e. a PET scan in coincidence mode for 15 min combined with a 30 min scan for the PALS measurement. The two-photon, i.e. standard coincidence, images were reconstructed with the vendor's TrueX reconstruction algorithm in ultra high sensitivity mode, including point-spread-function, attenuation, relative scatter and prompt photon corrections and with a 440 × 440 matrix, 4 iterations, 5 subsets. The resulting voxel size of the coincidence PET image is $1.9 \times 1.9 \times 1.65\,\mathrm{mm}^3$. For the PALS measurement, the scanner was operated in singles acquisition mode, a prototype feature to record every single-crystal interaction without the conventional two-photon coincidence sorting.

From the singles list-mode data, 3γE were identified using an offline prototype software. The detailed methodology is described in Ref. [21]. For the 3γE selection, the energy window for the annihilation photons is 460 keV to 545 keV and for the prompt photon 568 keV to 639 keV. The localization of the 3γE relies solely on the time-of-flight (TOF) information from the annihilation photons, i.e. no reconstruction algorithm like in Refs. [10,16–19,30,35] is used. The time window for the two annihilation photons is 4.2 ns. Spatial cuts, i.e. a minimal crystal distance, were also used to suppress random events arising from ^{176}Lu in Quadra's crystals.

Segmentations of volumes-of-interest (VOI) were performed either on the CT or coincidence PET images using LIFEx [36] and TotalSegmentator [37] and checked and/or amended by a nuclear medicine physician. We produced histoimages of the detected 3γE, i.e. images that visualize the total number of detected 3γE in a voxel, and verified that the VOI are visible. This serves as a consistency check to verify that the VOI contains more 3γE than the surrounding tissue, meaning we should not expect a large spill-in of 3γE. The six lesions of S1 are clearly visible in the histoimage. The other patients did not show regions with pathological uptake in the late scans. For the organ-level oPs lifetime determination, we considered the heart chambers, parotid glands, kidneys and liver in the early scans of all three patients. In the late scans, only the parotid glands and five lesions of S1 show enough 3γE to be considered for oPs lifetime fitting.

oPsLI was constructed with a voxel size of $7 \times 7 \times 7\,\mathrm{mm}^3$ on the late scan of S1 with a focus on the lesions and the early scan for S2. Though highly desirable from a clinical perspective, smaller voxel sizes do not seem to be very meaningful given the large positron range of ^{124}I (about 10 mm in water) and the absence of a true reconstruction algorithm for 3γE localization in our methodology. PAL spectra were generated by histogramming the measured delay between the prompt photon and the annihilation photons for each 3γE in a VOI or single voxel, as described in [21].

A three-component model was applied for fitting the measured PAL spectra. We consider three possible annihilation pathways: the positron may annihilate directly with an electron in the surrounding tissue, or it may first form pPs or oPs. The three exponential decay factors are convoluted with a Gaussian function that models the finite timing resolution of Quadra. The fit function for the PAL spectra is therefore

$$F = b + N \cdot \sum_{c=1}^{3} \frac{BR_c}{2\tau_c} e^{(\sigma^2 - 2t\tau_c + 2\Delta\tau_c)/(2\tau_c^2)} \cdot \mathrm{erfc}\left(\frac{\sigma}{\sqrt{2}\tau_c} + \frac{\Delta - t}{\sqrt{2}\sigma}\right). \quad (1)$$

In Eq. (1), b denotes the background and N is a normalization constant. $BR_{1,2,3}$ $\sum_{c=1}^{3} BR_c = 1$ are the relative branching ratios of pPs, direct annihilation and oPs, respectively, and τ_c are the corresponding lifetimes. σ and Δ are the parameters of the Gaussian function that models the timing resolution of the measurement. For an accurate estimate of the statistical uncertainties, our analysis relies on a Bayesian framework for the fitting of PAL spectra in single VOI or voxels outlined in Refs. [21–23]. We follow Ref. [23] for the definition of the prior distributions for the fit parameters. The values for the oPs lifetime τ_3 and the branching ratios $BR_{1,2,3}$ are consistent with the values reported for water by Ref. [38] with a broad spread of the distribution. The priors for the parameters σ and Δ follow the expectations we have for Quadra. Specifically, the priors are distributed as follows

$$\begin{aligned} \tau_3 &\sim \mathcal{N}(1.8\,\text{ns}, 0.8\,\text{ns}), \\ BR_{1,2,3} &\sim \text{Dirichlet}(0.75, 3.1, 1.15), \\ \sigma &\sim \mathcal{N}(0.1\,\text{ns}, 0.05\,\text{ns}), \\ \Delta &\sim \mathcal{N}(0.0\,\text{ns}, 0.5\,\text{ns}). \end{aligned} \tag{2}$$

The prior distribution for $BR_{1,2,3}$ in Eq. (2) yields 0.15, 0.62, and 0.23 as expectation values for the three branching ratios, which corresponds to the measurements of water [38]. The background b is fixed to the mean of the 3γE with time differences < -2 ns, while the fit is performed on time differences between -1.5 to 8.0 ns. We checked that there is no significant impact on the posterior distribution of τ_3 whether $\tau_{1,2}$ are fixed to literature values or considered as fit parameters with strong priors as in Ref. [23]. All errors are reported in terms of marginalized posterior distributions. While for τ_3 it is very similar to a Gaussian distribution, and hence quoting a standard deviation is acceptable, the relative component's BR need to be reported in terms of 68% highest-density-intervals (HDI).

Results

Fig. 1 shows the oPsLI of two coronal and axial slices in the region of the lesions. τ_3 and the statistical error $\Delta\tau_3$ were determined for $7 \times 7 \times 7\,\text{mm}^3$ voxels. In order to improve the visualization, in Fig. 1 the oPsLI was resampled and interpolated to the resolution of the coincidence PET image. Voxels with a relative standard deviation $< 65\%$ on 3γE with time differences < -2 ns were considered for τ_3 fitting. Applying the same condition as in Ref. [23], i.e. $< 20\%$, would leave too few voxels to fit. The PAL spectra of the two voxels with the highest number of 3γE are shown in the bottom row of Fig. 1.

The early scans of the three patients showed, unsurprisingly, most uptake in the gastrointestinal tract. With respect to oPsLI this is not particularly interesting. Nevertheless, Fig. 2 shows the oPsLI of S2 at 2 h post application.

Focusing our attention to the VOI-based analysis, Table 1 summarizes the lesions' properties, i.e. volume, mean voxel value within the VOI of the coincidence PET image and SUV_{max}, and if the lesion can be delineated on the FDG scan. The last column shows the oPs lifetime of the lesions. Clearly, the statistical uncertainty on τ_3 correlates with the mean activity concentration in the lesion (see also bottom right panel of Fig. 4). In Fig. 3 we visualize the PAL spectra of the lesions L1 to L4. L5 and L6 have the lowest count statistics and the PAL spectrum would be even worse than for L1. It should be noted that the PAL spectra are shown on a log scale and that the volume of the lesions under consideration is rather small. The top panel Fig. 4 shows the PAL spectra of all 3γE that were identified within the five lesions. As a reference, Table 2 reports the fit results for several VOI in the early scans of all three patients.

Finally, the bottom row Fig. 4 visualizes the dependence of $\Delta\tau_3$ on the maximal activity concentration in voxels of $7 \times 7 \times 7\,\text{mm}^3$ and on the mean activity contained in a VOI. For the voxel-based fit of the oPs lifetime, no significant correlation with the activity concentration from the coincidence PET can be established. However, for entire VOI it seems that the statistical precision does not improve significantly beyond an activity of $\mathcal{O}(100\,\text{kBq})$.

Discussion

^{124}I has been shown to be the prime candidate for oPsLI on Quadra [21–23]. On one side, the reasonably high prompt photon BR and its low energy make the 3γE selection algorithm from Ref. [21] and Quadra's detection capabilities less prone to random events. On the other side, [^{124}I]Iodide has very high and specific uptake in thyroid cancer lesions, despite having a lower activity that is administered to the patients compared to e.g. ^{68}Ga and ^{82}Rb. Because the differentiation of thyroid cancer lesions may be linked to oxygenation levels (see e.g. [33]), it could be relevant to utilize oPs lifetime measurements for a characterization of thyroid cancer lesions.

As in previous studies on in vivo oPs lifetime measurements, count statistics is the main challenge [20,22]. In order to distinguish oxygenation levels in tissue through the oPs lifetime, as e.g. investigated by Ref. [5], a high number of 3γE with large time differences $\gtrsim 2$ ns needs to be detected with a low random event rate. This is difficult to achieve with the current methodology under clinical conditions with respect to radionuclide, tracer, biokinetics, scan time, etc. Under conditions that are as good as it can possibly get from a clinical perspective (high uptake in S1's lesions), our study shows that voxel-wise determination of oPs lifetimes remains challenging. The right columns in Fig. 1 shows that even for the relatively large voxel size of $7\times7\times7\,\text{mm}^3$ the statistical uncertainty on τ_3 is too large to draw any clinically valuable information from the oPsLI. Longer scan time and/or higher administrated activities would improve statistics. However, this is difficult to achieve in clinical practice. For the PAL spectra in Fig. 1, only the voxel with the highest number of 3γE shows reasonable statistics and indeed the statistical error on τ_3 is "only" 14%. However, already for the "second best" voxel, the statistical error on τ_3 increases by almost a factor of two. In comparison, the activity concentration in the phantom measurements of Ref. [23] was about double the activity concentration we found in S1 at the maximal spot. The limiting factor with respect to oPsLI in this study is the size of the regions with activity concentrations of $\mathcal{O}(200\,\text{kBq}\,\text{mL}^{-1})$.

There does not seem to be a clear correlation between the maximal activity concentration in a voxel with the error on the oPs lifetime (see bottom left panel in Fig. 4). Likely this is because the activity concentration may correlate with the total number of 3γE, but not with the number of 3γE with large time differences, i.e. those events that dominate the fit of τ_3. Also, at the voxel level we are much more prone to mislocalizations of 3γE (spill-in/out of 3γE in a VOI). There may be also a significant uncertainty on the quantification in the coincidence PET image. As shown by Ref. [39], quantification of ^{124}I in small volumes is strongly affected by the suboptimal positron range correction of standard reconstruction algorithms. Possibly, different event selection and reconstruction algorithms and fitting procedures, as discussed in e.g. Refs. [10,16,18,19,30,35], may mitigate the problematic count statistics for oPsLI. In particular the proposed correction techniques for random 3γE may reduce the statistical uncertainty of τ_3. We leave the exploration of different reconstruction techniques on Quadra data sets to future studies.

If we measure the oPs lifetime at the level of single VOI rather than voxels, the statistical error on τ_3 drops significantly, compared to single voxels. Though we do not reach the precision of Ref. [23], L2 and L3 show a fairly good count statistics, as can be seen also in the PAL spectra of Fig. 3.

The results from Table 2 for the VOI-based fitting show that the oPs lifetimes are consistent with the lifetime in water within the statistical uncertainty [38]. τ_3 for the parotid glands seem to be consistently higher than for other organs, though still not statistically significant. We are unable to reach the precision on τ_3 that would be necessary to discriminate oxygenation levels investigated in Ref. [5] .

The VOI-based error on τ_3 shows a slight negative correlation with increasing mean activity in a VOI (see bottom right panel of Fig. 4). The correlation coefficient is $r = -0.48$ (95% credible interval

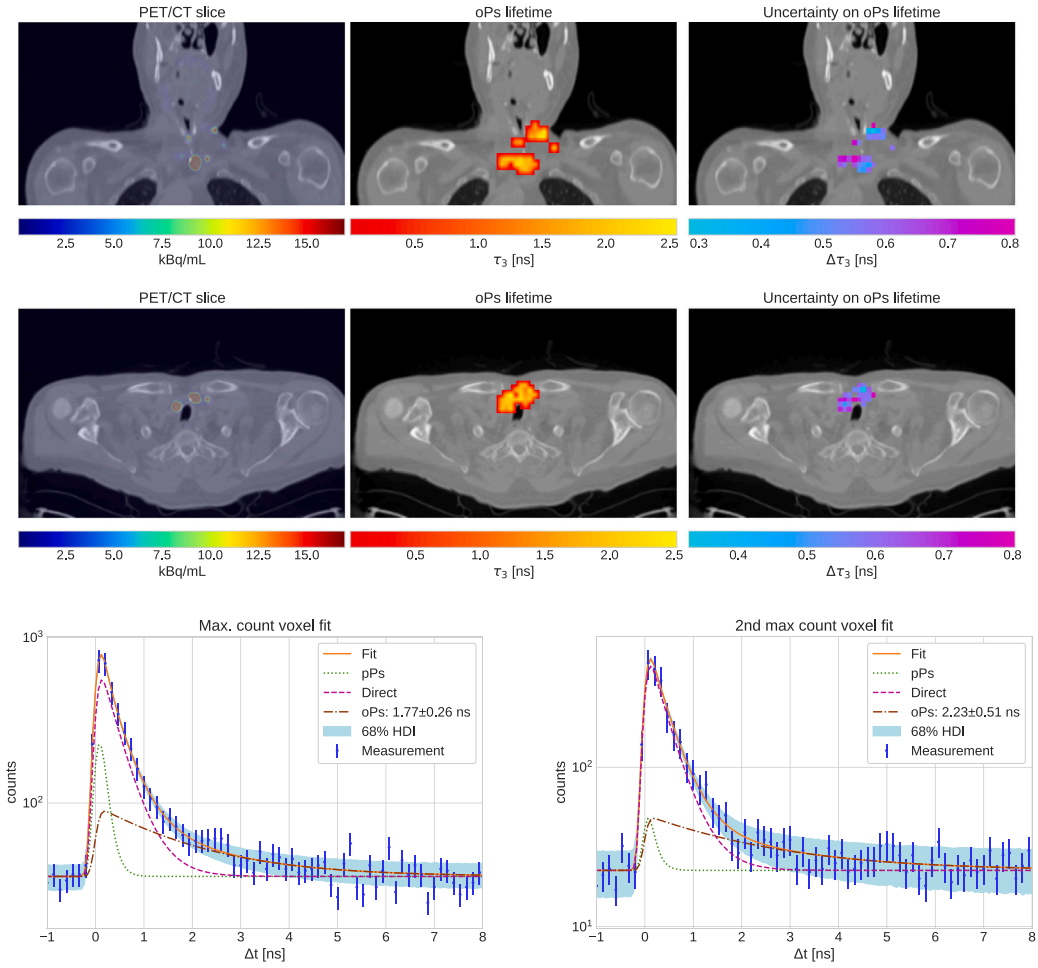

Fig. 1. oPsLI of coronal (*top row*) and axial (*center row*) slices of S1 in the region with lesions together with the coincidence PET slices (*left*) and the error voxel-wise error on τ_3 (*right*). For improved visualization, the τ_3 image was resampled and interpolated on the coincidence PET image resolution. The *bottom row* shows the PALS of the two voxels with the highest count statistics.

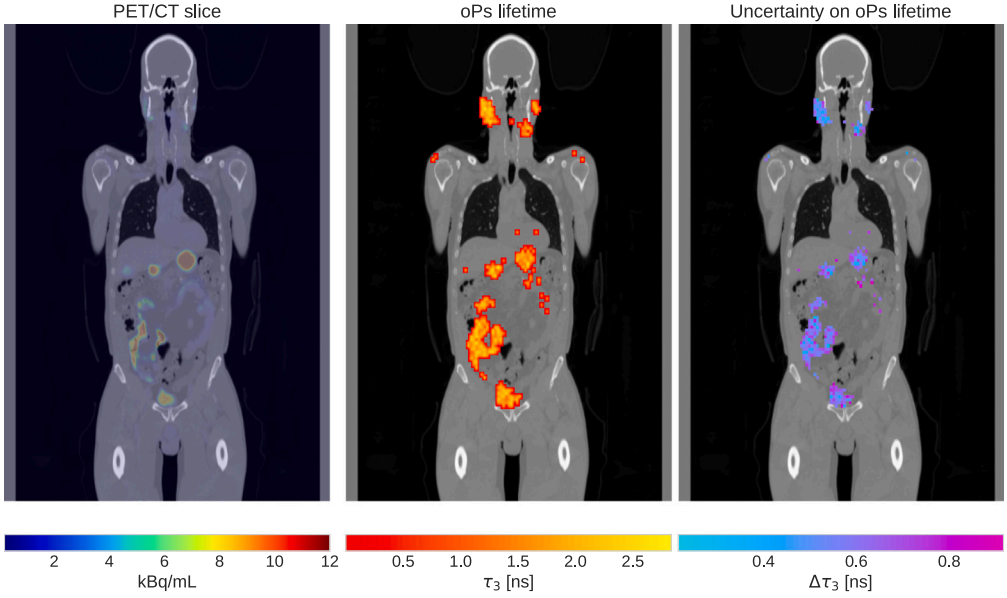

Fig. 2. A oPsLI coronal slice of S2's 2 h scan (*center*) together with the corresponding error on τ_3 (*right*) and coincidence PET image (*left*).

Table 1
Description and oPs lifetimes in S1's lesions. The activity from the ^{124}I coincidence scan is the mean voxel value in the lesions.

No.	Localization	FDG	Vol. [mL]	Act. [kBq mL^{-1}]	SUV$_{max}$	τ_3 [ns]
L1	Lymph node retropharyngeal	No	2.25	11.4	303.7	2.52 ± 0.48
L2	Left thyroid bed (cranial border)	No	4.33	18.5	526.2	1.83 ± 0.18
L3	Pretracheal lymph node	No	6.27	34.1	1028.2	1.91 ± 0.15
L4	Right paratracheal lymph node	Yes	3.39	16.1	191.7	2.32 ± 0.38
L5	Medial thyroid bed	No	1.31	9.5	25.9	1.77 ± 0.46
L6	Cervical left, border lymph node level IV/Vb	No	1.33	8.5	143.2	2.15 ± 0.58
–	All lesions	NA	18.88	22.0	1028.2	1.92 ± 0.11

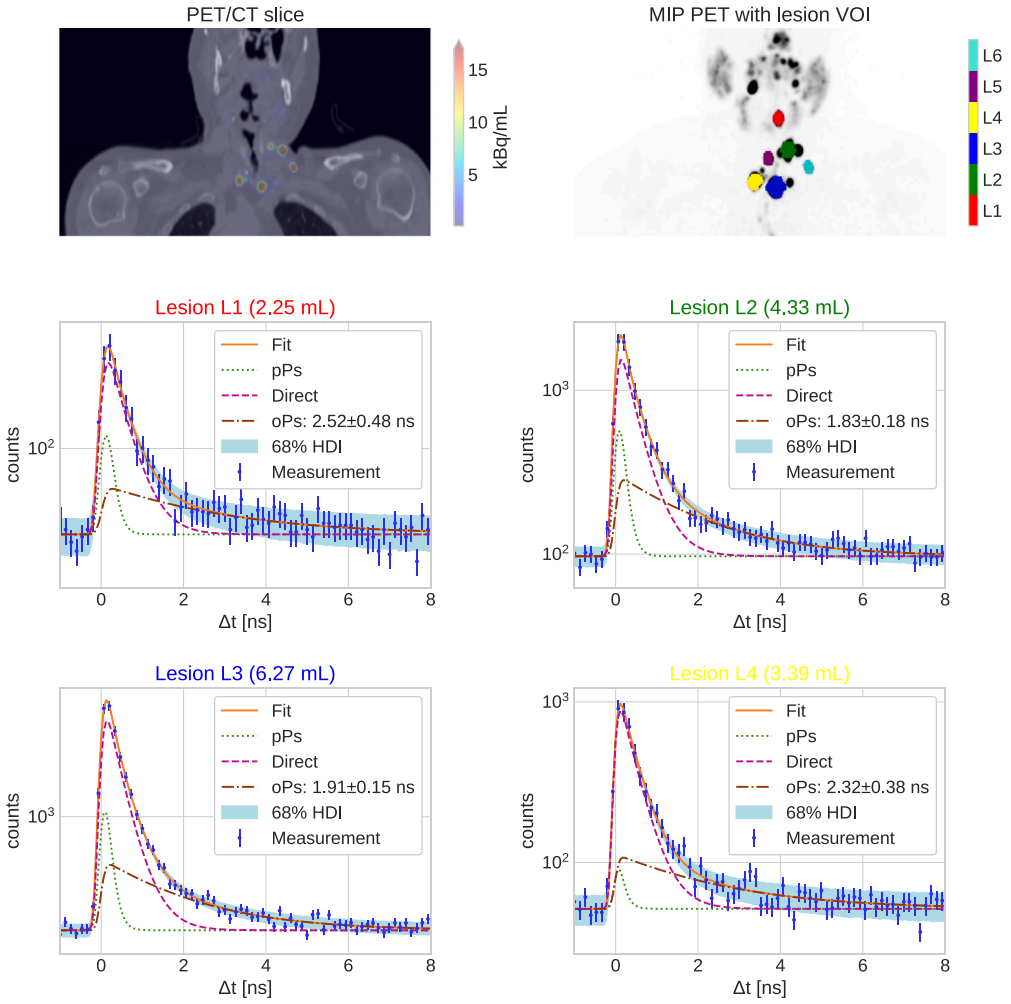

Fig. 3. The *top row* shows a slice of the coincidence PET/CT (*left*) and the MIP with the segmentation of the five lesions (*right*). The *center* and *bottom row* show PAL spectra of L1 to L4 of S1 at 26 h post application.

is $[-0.72, -0.15]$) with a Bayes factor of $BF_{10} = 7.88$. The spread of the points is still rather large, though. As discussed before, the mean activity might still not be the ideal surrogate quantity for the number of 3γE with large time differences above the background of random events.

Conclusions

The physical and biokinetic properties of ^{124}I make it the prime candidate for investigating oPsLI under clinical conditions with LAFOV PET/CT and the current methodology. For the first time, we showed the feasibility of oPs lifetime measurements in humans with ^{124}I on a commercial LAFOV PET/CT. It was shown that oPsLI of thyroid cancer patients can be achieved for the total body, but the 3γE count statistics remains a major challenge. In view of the expected oPs lifetime differences in different tissues and given our current methodology, the statistical uncertainty on τ_3 remains too large to yield any clinically useful information. Determining the oPs lifetime at the VOI level is practicable, though for some lesions the activity concentration and/or volume are on the lower end for achieving good count statistics. We hope that our study paves the way for more extensive studies for characterizing the differentiation of thyroid cancer metastases through oPs lifetime measurements, in particular using improved methodologies for 3γE selection and image reconstruction.

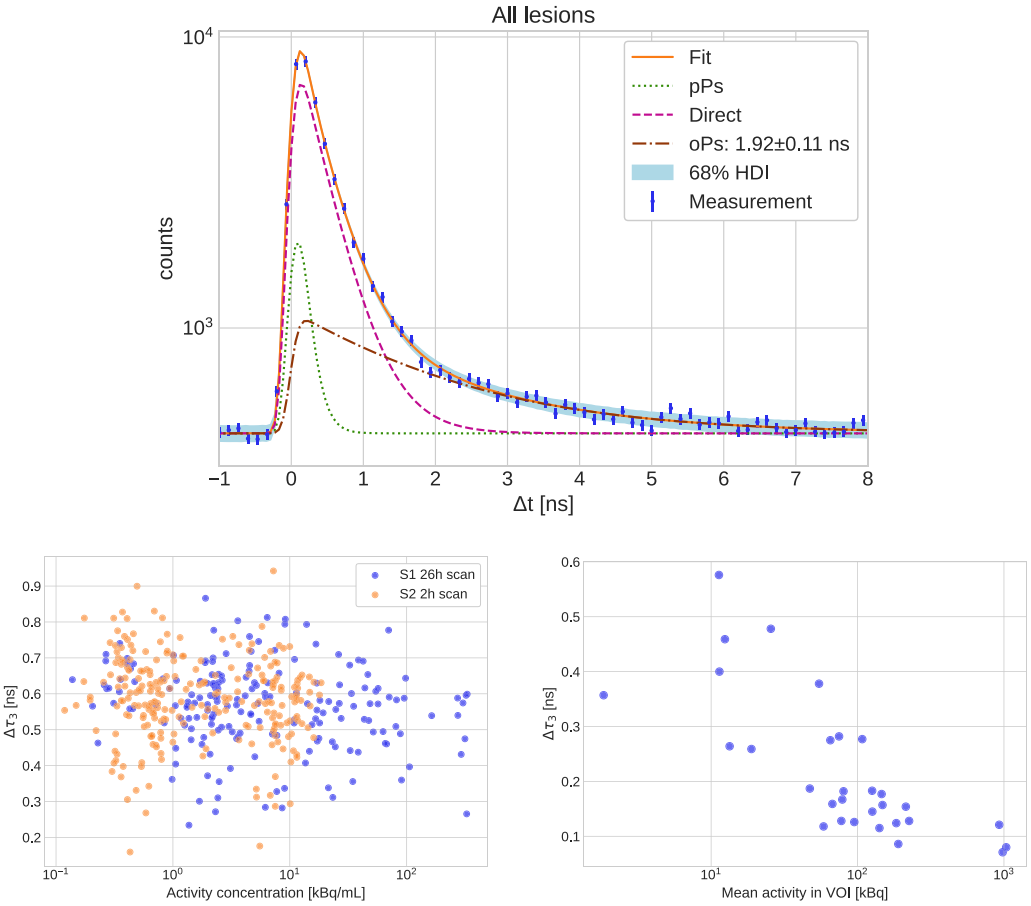

Fig. 4. *Top panel:* PALS of all 3γE within the lesions L1 to L5. *Bottom left:* Statistical uncertainty $\Delta\tau_3$ as a function of the activity concentration for individual voxels (color coded for S1's 26 h scan and S2's 2 h scan). *Bottom right:* Statistical uncertainty $\Delta\tau_3$ as a function of the total activity for each lesion of Table 1 and each VOI of Table 2.

Table 2
Fit results for all early scan VOI.

VOI	τ_3 [ns]	BR_1	HDI_{BR_1}	BR_2	HDI_{BR_2}	BR_3	HDI_{BR_3}
Left atrium S1	1.78 ± 0.28	0.01	[0.0, 0.01]	0.72	[0.7, 0.75]	0.27	[0.25, 0.29]
Left atrium S2	1.3 ± 0.19	0.01	[0.0, 0.01]	0.71	[0.69, 0.74]	0.28	[0.26, 0.3]
Left atrium S3	1.83 ± 0.17	0.01	[0.0, 0.01]	0.77	[0.76, 0.78]	0.22	[0.21, 0.23]
Right atrium S1	1.57 ± 0.28	0.01	[0.0, 0.01]	0.66	[0.64, 0.7]	0.33	[0.3, 0.35]
Right atrium S2	1.76 ± 0.16	0.01	[0.0, 0.01]	0.75	[0.74, 0.77]	0.24	[0.23, 0.25]
Right atrium S3	1.79 ± 0.13	0.01	[0.0, 0.01]	0.76	[0.75, 0.77]	0.23	[0.22, 0.24]
Left parotid gland S1	1.92 ± 0.13	0.13	[0.12, 0.14]	0.6	[0.58, 0.62]	0.27	[0.26, 0.28]
Left parotid gland S2	2.64 ± 0.4	0.1	[0.08, 0.13]	0.62	[0.59, 0.66]	0.27	[0.26, 0.29]
Left parotid gland S2	2.64 ± 0.4	0.1	[0.08, 0.13]	0.62	[0.59, 0.66]	0.27	[0.26, 0.29]
Right parotid gland S1	2.24 ± 0.12	0.08	[0.07, 0.09]	0.65	[0.64, 0.66]	0.27	[0.27, 0.28]
Right parotid gland S2	2.25 ± 0.26	0.03	[0.02, 0.05]	0.71	[0.69, 0.74]	0.25	[0.24, 0.27]
Right parotid gland S2	2.25 ± 0.26	0.03	[0.02, 0.05]	0.71	[0.69, 0.74]	0.25	[0.24, 0.27]
Left kidney S1	1.37 ± 0.28	0.01	[0.0, 0.01]	0.62	[0.59, 0.68]	0.37	[0.32, 0.4]
Left kidney S2	1.92 ± 0.18	0.0	[0.0, 0.0]	0.72	[0.71, 0.74]	0.27	[0.26, 0.28]
Left kidney S3	1.87 ± 0.12	0.01	[0.0, 0.01]	0.75	[0.74, 0.76]	0.25	[0.24, 0.26]
Right kidney S1	1.32 ± 0.18	0.01	[0.0, 0.01]	0.61	[0.58, 0.64]	0.38	[0.35, 0.41]
Right kidney S2	1.6 ± 0.14	0.01	[0.0, 0.01]	0.71	[0.7, 0.73]	0.28	[0.27, 0.3]
Right kidney S3	1.96 ± 0.13	0.01	[0.0, 0.02]	0.74	[0.73, 0.76]	0.25	[0.24, 0.25]
Liver S1	1.53 ± 0.12	0.01	[0.0, 0.01]	0.7	[0.68, 0.71]	0.3	[0.28, 0.31]
Liver S2	1.68 ± 0.08	0.0	[0.0, 0.0]	0.74	[0.73, 0.74]	0.26	[0.26, 0.27]
Liver S3	1.78 ± 0.07	0.01	[0.0, 0.0]	0.74	[0.74, 0.75]	0.25	[0.25, 0.26]
Spleen S1	1.28 ± 0.16	0.01	[0.0, 0.01]	0.64	[0.62, 0.68]	0.35	[0.32, 0.37]
Spleen S2	1.61 ± 0.12	0.01	[0.0, 0.01]	0.73	[0.72, 0.75]	0.26	[0.25, 0.27]
Spleen S3	1.68 ± 0.09	0.01	[0.0, 0.01]	0.75	[0.74, 0.76]	0.24	[0.24, 0.25]

CRediT authorship contribution statement

Lorenzo Mercolli: Writing – review & editing, Writing – original draft, Visualization, Validation, Project administration, Methodology, Investigation, Funding acquisition, Formal analysis, Data curation, Conceptualization. **William M. Steinberger:** Writing – review & editing, Software, Methodology, Formal analysis. **Tilman Läppchen:** Resources, Project administration. **Michelle Amon:** Resources. **Carola Bregenzer:** Resources. **Maurizio Conti:** Software. **Ângelo R. Felgosa Cardoso:** Resources, Conceptualization. **Clemens Mingels:** Resources. **Paweł Moskal:** Funding acquisition. **Narendra Rathod:** Resources. **Hasan Sari:** Software. **Ewa Ł. Stępień:** Funding acquisition. **Sabine Weidner:** Resources. **Axel Rominger:** Funding acquisition. **Kuangyu Shi:** Funding acquisition. **Robert Seifert:** Writing – review & editing, Supervision, Project administration, Conceptualization.

Consent to participate

Informed consent was obtained from all individual participants included in the study.

Ethics approval

This study was performed in line with the principles of the Declaration of Helsinki. All patients provided written informed consent for the use of anonymized imaging data for research purposes.

Funding

This research is partially supported by the grant no. 216944 under the Weave/Lead Agency program of the Swiss National Science Foundation, Switzerland and the National Science Centre of Poland through grant OPUS24+LAP No. 2022/47/I/NZ7/03112.

Declaration of competing interest

The authors declare the following financial interests/personal relationships which may be considered as potential competing interests: William M. Steinberger reports financial support was provided by Siemens Medical Solutions USA Inc. Maurizio Conti reports financial support was provided by Siemens Medical Solutions USA Inc. Hasan Sari reports financial support was provided by Siemens Healthineers AG. Axel Rominger reports: financial support and travel were provided by Siemens Healthineers AG; he is Associate Editor of EANM Innovation, but had no involvement in the peer review process or manuscript decisions. Robert Seifert reports a relationship with Novartis AG that includes: speaking and lecture fees. Robert Seifert reports a relationship with Boston Scientific Corporation that includes: speaking and lecture fees. Robert Seifert reports a relationship with Else Kroner-Fresenius Foundation that includes: funding grants. Robert Seifert reports a relationship with Boehringer Ingelheim Fonds Foundation for Basic Research in Medicine that includes: funding grants. Kuangyu Shi reports a relationship with Novartis that includes: funding grants. Kuangyu Shi reports a relationship with Siemens Healthineers AG that includes: funding grants and speaking and lecture fees. Kunagyu Shi reports a relationship with United Imaging Healthcare Co., Ltd. that includes: speaking and lecture fees. Kuangyu Shi reports a relationship with Subtle Medical that includes: speaking and lecture fees. Pawel Moskal has patent #PL 227658; EP 3039453; US 9,851,456 issued to Pawel Moskal. If there are other authors, they declare that they have no known competing financial interests or personal relationships that could have appeared to influence the work reported in this paper.

Acknowledgment

All authors read and approved the final manuscript.

Data availability

Data will be made available on request.

References

[1] Moskal P. Positronium imaging. In: 2019 IEEE nuclear science symposium and medical imaging conference. 2019, p. 1–3.

[2] Das M, Sharma S, Beyene EY, Bilewicz A, Choinski J, Chug N, Curceanu C, Czerwinski E, Eliyan KV, Hajduga J, Jalali S, Kacprzak K, Kaplanoglu T, Kaplon L, Kasperska K, Khreptak A, Korcyl G, Kozik T, Kubat K, Kumar D, Venadan AK, Lisowski E, Lisowski F, Medrala-Sowa J, Moyo S, Mryka W, Niedźwiecki S, Pandey P, Parzych S, Porcelli A, Rachwal B, del Rio EP, Rädler M, Rominger A, Shi K, Skurzok M, Stolarz A, Szumlak T, Tanty P, Ardebili KT, Tiwari S, Walczak R, Stepien EL, Moskal P. First positronium imaging using 44sc with the J-PET scanner: a case study on the NEMA-image quality phantom. IEEE Trans Radiat Plasma Med Sci 2025. 1–1.

[3] Moskal P, Kisielewska D, Curceanu C, Czerwiński E, Dulski K, Gajos A, Gorgol M, Hiesmayr B, Jasińska B, Kacprzak K, Kapłon Ł, Korcyl G, Kowalski P, Krzemień W, Kozik T, Kubicz E, Mohammed M, Niedźwiecki S, Pałka M, Pawlik-Niedźwiecka M, Raczyński L, Raj J, Sharma S, Shivani, Shopa RY, Silarski M, Skurzok M, Stępień E, Wiślicki W, Zgardzińska B. Feasibility study of the positronium imaging with the J-PET tomograph. Phys Med Biol 2019;64:055017.

[4] Moskal P, Jasińska B, Stępień EŁ, Bass SD. Positronium in medicine and biology. Nat Rev Phys 2019;1(9):527–9.

[5] Shibuya K, Saito H, Nishikido F, Takahashi M, Yamaya T. Oxygen sensing ability of positronium atom for tumor hypoxia imaging. Commun Phys 2020;3:173.

[6] Stepanov PS, Selim FA, Stepanov SV, Bokov AV, Ilyukhina OV, Duplâtre G, Byakov VM. Interaction of positronium with dissolved oxygen in liquids. Phys Chem Chem Phys: PCCP 2020;22:5123–31.

[7] Stepanov SV, Byakov VM, Stepanov PS. Positronium in biosystems and medicine: A new approach to tumor diagnostics based on correlation between oxygenation of tissues and lifetime of the positronium atom. Phys Wave Phenom 2021;29.

[8] Moskal P, Dulski K, Chug N, Curceanu C, Czerwiński E, Dadgar M, Gajewski J, Gajos A, Grudzień G, Hiesmayr BC, Kacprzak K, Kapł on Ł, Karimi H, Klimaszewski K, Korcyl G, Kowalski P, Kozik T, Krawczyk N, Krzemień W, Kubicz E, Małczak P, Niedźwiecki S, Pawlik-Niedźwiecka M, Pędziwiatr M, Raczyński L, Raj J, Ruciński A, Sharma S, Shivani, Shopa RY, Silarski M, Skurzok M, Stępień EŁ, Szczepanek M, Tayefi F, Wiślicki W. Positronium imaging with the novel multiphoton PET scanner. Sci Adv 2021;7:eabh4394.

[9] Moskal P, Stępień EŁ. Positronium as a biomarker of hypoxia. Bio-Algorithms Med-Syst 2021;17(4):311–9.

[10] Qi J, Huang B. Positronium lifetime image reconstruction for TOF PET. IEEE Trans Med Imaging 2022;41:2848–55.

[11] Bass SD, Mariazzi S, Moskal P, Stępień EŁ. Colloquium: Positronium physics and biomedical applications. Rev Modern Phys 2023;95:021002, Available from: URL https://link.aps.org/doi/10.1103/RevModPhys.95.021002.

[12] Hourlier A, Boisson F, Brasse D. Experimental uses of positronium and potential for biological applications. IEEE Trans Radiat Plasma Med Sci 2024;8(6):581–94.

[13] Takyu S, ichiro Matsumoto K, Hirade T, Nishikido F, Akamatsu G, Tashima H, Takahashi M, Yamaya T. Quantification of radicals in aqueous solution by positronium lifetime: an experiment using a clinical PET scanner. Japan J Appl Phys 2024;63(8):086003. http://dx.doi.org/10.35848/1347-4065/ad679a.

[14] Shimazoe K, Donghwan K, Mineo T, Sato T, Ohta S, Tatsumi T, Sugiyama A, Yamatsugu K, Nomura S, Terabayashi R, et al. pH dependence of perturbed angular correlation in DOTA chelated 111 in measured with ring-shape gamma-ray detectors. Interactions 2024;245(1):22.

[15] Tashima H, Yamaya T. Three-Gamma imaging in nuclear medicine: A review. IEEE Trans Radiat Plasma Med Sci 2024;8(8):853–66.

[16] Huang B, Li T, Arino-Estrada G, Dulski K, Shopa RY, Moskal P, Stepien E, Qi J. SPLIT: Statistical positronium lifetime image reconstruction via time-thresholding. IEEE Trans Med Imaging 2024;43:2148–58.

[17] Huang B, Qi J. High-resolution positronium lifetime tomography by the method of moments. Phys Med Biol 2024;69(24):24NT01.

[18] Chen Z, Kao C-M, Huang H-H, An L. Enhanced positronium lifetime imaging through two-component reconstruction in time-of-flight positron emission tomography. Front Phys 2024;12:1429344.

[19] Huang B, Dai B, Lapi SE, Liles G, Karp JS, Qi J. High-resolution positronium lifetime tomography at clinical activity levels on the PennPET explorer. J Nucl Med 2025;66(9):1464–70.

[20] Moskal P, Baran J, Bass S, Choiński J, Chug N, Curceanu C, Czerwiński E, Dadgar M, Das M, Dulski K, Eliyan KV, Fronczewska K, Gajos A, Kacprzak K, Kajetanowicz M, Kaplanoglu T, Kapłon Ł, Klimaszewski K, Kobylecka M, Korcyl G, Kozik T, Krzemień W, Kubat K, Kumar D, Kunikowska J, Mączewska J, Migdał W, Moskal G, Mryka W, Niedźwiecki S, Parzych S, del Rio EP, Raczyński L, Sharma S, Shivani S, Shopa RY, Silarski M, Skurzok M, Tayefi F, Ardebili KT, Tanty P, Wiślicki W, Królicki L, Stępień EŁ. Positronium image of the human brain in vivo. Sci Adv 2024;10(37):eadp2840, Available from: URL https://www.medrxiv.org/content/early/2024/02/03/2024.02.01.23299028.

[21] Steinberger WM, Mercolli L, Breuer J, Sari H, Parzych S, Niedzwiecki S, Lapkiewicz G, Moskal P, Stępień EŁ, Rominger A, Shi K, Conti M. Positronium lifetime validation measurements using a long-axial field-of-view positron emission tomography scanner. EJNMMI Phys 2024;11(76).

[22] Mercolli L, Steinberger WM, Sari H, Afshar-Oromieh A, Caobelli F, Conti M, Felgosa Cardoso ÂR, Mingels C, Moskal P, Pyka T, Rathod N, Schepers R, Seifert R, Shi K, Stępień EŁ, Viscione M, Rominger AO. In vivo positronium lifetime measurements with a long axial field-of-view PET/CT. Cold Spring Harbor Laboratory Press; 2024, Available from: URL https://www.medrxiv.org/content/early/2024/10/22/2024.10.19.24315509, MedRxiv.

[23] Mercolli L, Steinberger WM, Rathod N, Conti M, Moskal P, Rominger A, Seifert R, Shi K, Stępień EŁ, Sari H. Phantom imaging demonstration of positronium lifetime with a long axial field-of-view PET/CT and (124)I. EJNMMI Phys 2025;12:80.

[24] Mercolli L, Steinberger WM, Grundler PV, Moiseeva A, Braccini S, Conti M, Moskal P, Rathod N, Rominger A, Sari H, Schibli R, Seifert R, Shi K, Stępień EŁ, van der Meulen NP. First positronium lifetime imaging with scandium-44 on a long axial field-of-view PET/CT. Front Nucl Med 2025;5:1648621.

[25] Süvegh K, Marek T. Positron annihilation spectroscopies. In: Vértes A, Nagy S, Klencsár Z, Lovas RG, Rösch F, editors. Handbook of nuclear chemistry. Boston, MA: Springer US; 2011, p. 1461–84.

[26] Conti M, Eriksson L. Physics of pure and non-pure positron emitters for PET: a review and a discussion. EJNMMI Phys 2016;3:8.

[27] Spencer BA, Berg E, Schmall JP, Omidvari N, Leung EK, Abdelhafez YG, Tang S, Deng Z, Dong Y, Lv Y, Bao J, Liu W, Li H, Jones T, Badawi RD, Cherry SR. Performance evaluation of the uEXPLORER total-body PET/CT scanner based on NEMA NU 2-2018 with additional tests to characterize PET scanners with a long axial field of view. J Nucl Med 2021;62:861–70.

[28] Prenosil GA, Sari H, Fürstner M, Afshar-Oromieh A, Shi K, Rominger A, Hentschel M. Performance characteristics of the biograph vision quadra PET/CT system with a long axial field of view using the NEMA NU 2-2018 standard. J Nucl Med 2022;63:476–84.

[29] Dai B, Daube-Witherspoon ME, McDonald S, Werner ME, Parma MJ, Geagan MJ, Viswanath V, Karp JS. Performance evaluation of the pennpet explorer with expanded axial coverage. Phys Med Biol 2023;68(9):095007.

[30] Shibuya K, Saito H, Tashima H, Yamaya T. Using inverse Laplace transform in positronium lifetime imaging. Phys Med Biol 2022;67(2):025009.

[31] Jegal J, Jeong D, Seo E-S, Park H, Kim H. Convolutional neural network-based reconstruction for positronium annihilation localization. Sci Rep 2022;12:8531.

[32] Shopa RY, Dulski K. Positronium imaging in J-PET with an iterative activity reconstruction and a multi-stage fitting algorithm. Bio-Algorithms Med-Syst 2023;19(1):54–63.

[33] Ma B, Wen S, Luo Y, Zhang T, Yang Y, Shen C, Zhang Y, Ji Q, Qu N, Wang Y. Targeting tumor hypoxia inhibits aggressive phenotype of dedifferentiated thyroid cancer. J Clin Endocrinol Metab 2022;108(2):368–84.

[34] Jentzen W, Freudenberg L, Eising EG, Sonnenschein W, Knust J, Bockisch A. Optimized 124I PET dosimetry protocol for radioiodine therapy of differentiated thyroid cancer. J Nucl Med 2008;49(6):1017–23.

[35] Chen Z, An L, Kao C-M, Huang H-H. The properties of the positronium lifetime image reconstruction based on maximum likelihood estimation. Bio-Algorithms Med-Syst 2023;19(1):1–8.

[36] Nioche C, Orlhac F, Boughdad S, Reuzé S, Goya-Outi J, Robert C, Pellot-Barakat C, Soussan M, Frouin F, Buvat I. LIFEx: a freeware for radiomic feature calculation in multimodality imaging to accelerate advances in the characterization of tumor heterogeneity (RRID:SCR_025284). Cancer Res 2018;78(16):4786–9.

[37] Wasserthal J, Breit H-C, Meyer MT, Pradella M, Hinck D, Sauter AW, Heye T, Boll DT, Cyriac J, Yang S, Bach M, Segeroth M. TotalSegmentator: Robust segmentation of 104 anatomic structures in CT images. Radiol: Artif Intell 2023;5(5):e230024, Available from: URL https://doi.org/10.1148/ryai.230024.

[38] Kotera K, Saito T, Yamanaka T. Measurement of positron lifetime to probe the mixed molecular states of liquid water. Phys Lett A 2005;345(1):184–90, Available from: URL https://www.sciencedirect.com/science/article/pii/S0375960105011035.

[39] Kertész H, Conti M, Panin V, Cabello J, Bharkhada D, Beyer T, Papp L, Jentzen W, Cal-Gonzalez J, Herraiz JL, López-Montes A, Rausch I. Positron range in combination with point-spread-function correction: an evaluation of different implementations for [124I]-PET imaging. EJNMMI Phys 2022;9(1):56.